ADVANCED FUNCTIONAL MATERIALS
www.afm-journal.de

Materials Views
www.MaterialsViews.com

High-Performance Flexible Multilayer MoS_2 Transistors on Solution-Based Polyimide Substrates

Won Geun Song, Hyuk-Jun Kwon, Jozeph Park, Junyeob Yeo, Minjeong Kim, Suntak Park, Sungryul Yun, Ki-Uk Kyung, Costas P. Grigoropoulos, Sunkook Kim,* and Young Ki Hong**

Transition metal dichalcogenides (TMDs) layers of molecular thickness, in particular molybdenum disulfide (MoS_2), become increasingly important as active elements for mechanically flexible/stretchable electronics owing to their relatively high carrier mobility, wide bandgap, and mechanical flexibility. Although the superior electronic properties of TMD transistors are usually integrated into rigid silicon wafers or glass substrates, the achievement of similar device performance on flexible substrates remains quite a challenge. The present work successfully addresses this challenge by a novel process architecture consisting of a solution-based polyimide (PI) flexible substrate in which laser-welded silver nanowires are embedded, a hybrid organic/inorganic gate insulator, and multilayers of MoS_2. Transistors fabricated according to this process scheme have decent properties: a field-effect-mobility as high as 141 cm^2 V^{-1} s^{-1} and an I_{on}/I_{off} ratio as high as 5×10^5. Furthermore, no apparent degradation in the device properties is observed under systematic cyclic bending tests with bending radii of 10 and 5 mm. Overall electrical and mechanical results provide potentially important applications in the fabrication of versatile areas of flexible integrated circuitry.

1. Introduction

The ever-increasing interaction between human beings and electronic devices requires the development of robust flexible electronics, which can endure harsh environments that may induce considerable mechanical bending, folding, and stretching.[1] Research is being conducted worldwide on the development of bendable/foldable or stretchable devices of high performance and mechanical stability.[1c,2] The latter allows realization of flexible displays,[3] flexible energy storage devices,[4] and flexible sensors that detect various mechanical, optoelectrical, environmental, and biological stimuli.[5] Such lightweight devices in the form of soft films may ultimately be implemented in wearable electronics or on the human body in the form of smart skins. These human-friendly applications are attracting substantial interest.[6]

Key challenges in the fabrication of such flexible electronic devices arise from the fact that the basic components forming unit thin film transistors (TFTs) must be stable with respect to various mechanical stresses. The individual layers that constitute TFTs such as gate electrodes, gate insulators (GI), and source/drain (S/D) electrodes must be both mechanically and electrically stable with respect to external stresses. Especially, semiconductors such as amorphous silicon (*a*-Si:H) and low temperature poly-silicon are prone to deterioration upon bending, thus alternative materials are under consideration. In this regard, 2D transition metal dichalcogenides, such as molybdenum disulfide (MoS_2), exhibit high mechanical flexibility (Young's modulus 240–270 GPa) owing to their 2D nanosheet structure.[1c,7] Also, their relatively high carrier mobility (>100 cm^2 V^{-1} s^{-1}) and wide bandgap (1.3 eV < E_g < 1.9 eV) make them an attractive candidate for the fabrication of high performance flexible devices.[8]

Second, in order to fabricate flexible devices using conventional thin-film processes, the use of flexible substrates that may endure relatively high temperature (up to ≈500 °C, which is a typical process temperature of Si TFT technology) is necessary. The most commonly used flexible substrates include poly(methyl methacrylate) (PMMA), polyether sulfone, polyethylene naphthalate (PEN), polyethylene terephthalate (PET), and polyimide (PI).[3c] However, most of the above easily warp during high temperature processing, except PI substrates that exhibit decomposition temperatures close to 600 °C as well as

W. G. Song, Dr. J. Park,[+] M. Kim, Prof. S. Kim, Dr. Y. K. Hong
Multi-Functional Nano/Bio Electronics Lab
Kyung Hee University
Gyeonggi 446-701, Republic of Korea
E-mail: intel0616@gmail.com; imhyke@khu.ac.kr
Dr. H.-J. Kwon, Dr. J. Yeo, Prof. C. P. Grigoropoulos
Laser Thermal Lab
Department of Mechanical Engineering
University of California
Berkeley, CA 94720, USA
E-mail: cgrigoro@berkeley.edu
Dr. S. Park, Dr. S. Yun, Dr. K.-U. Kyung
Transparent Transducer and UX Creative Research Center
Electronics and Telecommunications Research Institute
Daejeon 305-700, Republic of Korea
[+]Present address: Samsung Display, Inc., Yongin-Si 446-920, Republic of Korea

DOI: 10.1002/adfm.201505019

 © 2016 WILEY-VCH Verlag GmbH & Co. KGaA, Weinheim

high chemical/mechanical stability.[3c,9] Solution type PI may be spin-coated onto rigid carrier glasses, and flexible devices may be fabricated thereon. For instance, TFTs incorporating MoS_2 necessitate high temperature annealing (>250 °C) in order to reduce the contact resistance between the S/D electrodes and the semiconductor.[8c,d] Thus, PI substrates are appropriate for the fabrication of high performance flexible devices.

Many research groups have struggled to find alternative conductive flexible electrodes, since the usual metal films are rather ductile and require expensive vacuum deposition techniques. Several candidates have been studied and introduced up to date, including highly conductive poly(3,4-ethylenedioxythiophene):poly(4-styrenesulfonate),[10] metal grids,[11] graphene,[12] carbon nanotubes,[13] nanotube–polymer composites,[14] and silver nanowire (Ag NW) meshes.[15] Among the suggested materials, 2D random networks of Ag NWs are promising because of their compatibility with cost-effective solution processes and the reasonably high electrical conductivity. However, random network of Ag NWs may be inappropriate for practical applications.[16] First, the electrical properties must be preserved upon mechanical bending or stretching. Next, the surface roughness of the entire electrode layer must be sufficiently small in order to guarantee fast carrier transport along the active layers grown above them. Finally, the NWs must adhere well to the substrate and form contacts at their intersections.

The electrical contact at the Ag NW junctions can be improved by laser welding,[17] which is based on highly localized heating induced by plasmonic effects.[18] Such a treatment makes conductivities of the Ag NW films less susceptible to external mechanical stress, but considerable surface roughness still persists. A possible solution to this issue is to embed the Ag NW electrode into the substrate, which also eliminates the film–substrate adhesion problem.

The process presented herein achieves mechanically flexible MoS_2 TFT devices of high electrical performance. 2D multilayer MoS_2 is used as the active channel, while laser-welded Ag NWs networks are embedded in flexible PI substrates serving as gate electrodes. Solution-based PI can be spin-coated over the Ag NW network, resulting in smooth surface topography of the overlaying stack. In order to decrease the contact resistance at the NW junctions, laser welding is performed so as to obtain high conductivity of the Ag NW network (10–15 Ω sq^{-1}, almost 37 or 55-fold decrease). As a result, the conductivity of the Ag NW electrodes is preserved, even under mechanical bending while peeling effects are reduced. Owing to the high reliability of PI substrates with respect to thermal budget, the relatively high Schottky barrier between MoS_2 and S/D electrodes can be reduced by annealing at elevated temperature. Field effect mobility (μ_{eff}) values of ≈141 cm^2 V^{-1} s^{-1} are obtained, with a high current on/off ratio (I_{on}/I_{off}) of 5×10^5. Nonlinear hyperelastic simulations allow estimation of mechanical stress in the flexible devices with respect to the radius of curvature and film thickness, which is useful for determining practical design limits. It is predicted that devices with a total thickness of 0.1 mm can endure a bending radius of upt to 2.5 mm. For a bending radius of 5 mm, the total allowed thickness for a stable device increases up to ≈0.85 mm. Static bending tests confirm stable transistor performance over a relatively broad range of bending radii (up to 5 mm). The electrical and mechanical stability is further evaluated through a cyclic bending test (1000 cycles).

2. Results and Discussion

2.1. Fabrication Platform of Flexible Device

Figure 1a shows a schematic flow chart of the fabrication procedure for a flexible TFT platform consisting of laser welded/embedded 2D Ag NWs network and solution-based thin PI, and organic/inorganic hybrid GI. First, 2D random network of Ag NWs as a flexible gate electrode is created by a vacuum filtration method so as to minimize the agglomeration of NWs by using a very small amount of NW solution (25 µL). The Ag NWs are then deposited uniformly onto the surface. The filtrated Ag NWs are interconnected forming mesh-like arrangement (circle shape with 40 mm diameter). In order to enhance the electrical property, a laser beam with 532 nm wavelength is irradiated onto the Ag NWs network. The ensuing plasmonic laser welding process will be discussed later in detail. For a flexible substrate, solution-type PI is spin-coated onto the laser-treated Ag NWs network, resulting in the permeation of PI into the voids formed between the Ag NWs owing to its low viscosity and surface energy. As a result, the Ag NWs are partially embedded and held firmly within the flexible PI substrate with their initial positions and corresponding contacts remaining intact under varying mechanical stress. This partially embedded structure also guarantees a damage-free detachment of the 2D Ag NWs network/PI composite from the substrate. No sacrificial layer or excimer laser treatment is necessary for this process, which would otherwise require expensive tools while possibly inducing damage in the devices from residual solvent or burnt residue.[7b,19] It should be noted that sheet resistance of the as-detached Ag NWs network, which is partially embedded in the PI, remained almost identical to that measured after the laser-welding procedure. After the detachment, the flexible PI layer containing Ag NWs is mechanically fixed on a carrier substrate (Glass-2 in Figure 1a). The carrier substrate is used to undergo a conventional TFT fabrication procedure including photolithography, metallization, lift-off/etching, and post-thermal treatment. To fabricate an organic/inorganic hybrid GI, organic material (SU-8 2000.5), instead of the conventional oxide-based counterparts, is spin-coated onto the surface where Ag NWs are partially exposed, resulting in a bilaterally embedded sandwich structure (e.g., SU-8/Ag NWs/PI), which could reinforce the advantages of partial-embedded structure and enhance the mechanical flexibility of the final device.[20] High-*k* aluminum oxide (Al_2O_3) is deposited next onto the SU-8 layer by atomic layer deposition (ALD). The inorganic dielectric provides high insulating properties, while also compensating the rather poor adhesion between the hydrophobic organic surface and subsequent multilayered MoS_2 and metal S/D electrodes. The multilayer MoS_2 TFT array is fabricated based on previous reports by the authors (see the Experimental Section for more details).[8c,d] After optimizing the electrical contact properties between the active layer and the S/D electrodes by post-thermal annealing, the TFT array is

© 2016 WILEY-VCH Verlag GmbH & Co. KGaA, Weinheim

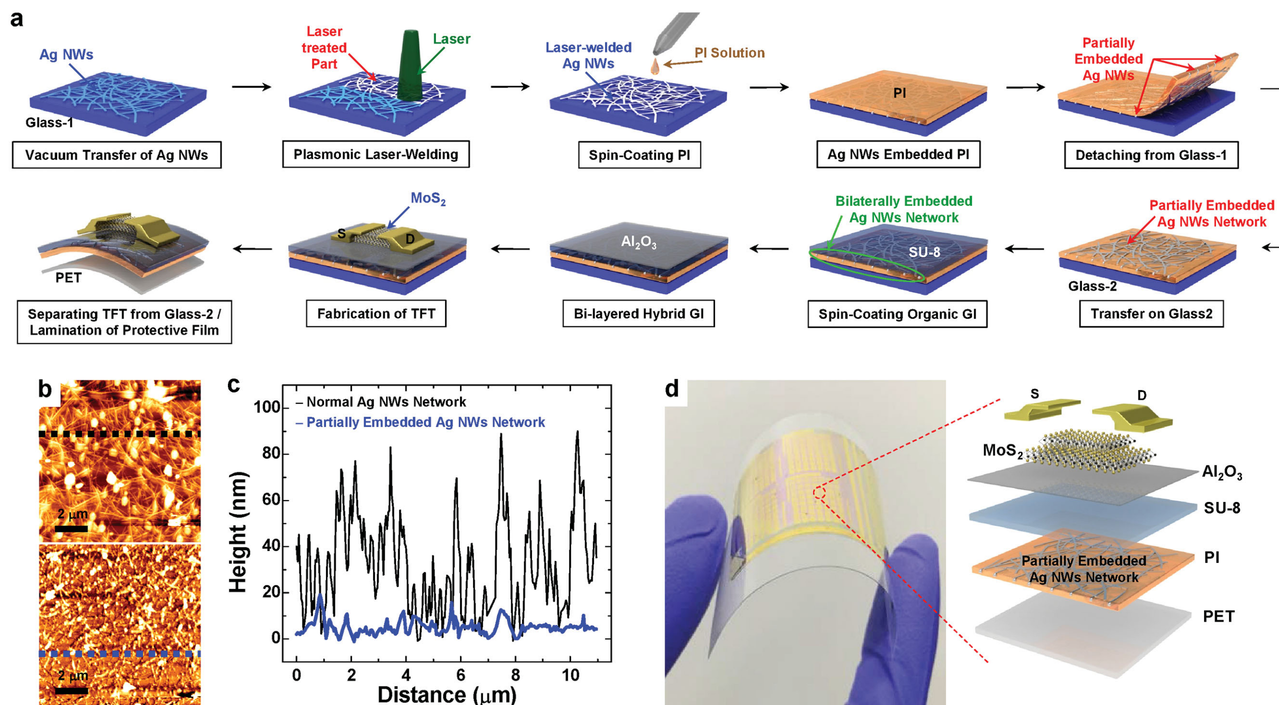

Figure 1. Flexible multilayer MoS_2 TFTs. a) Schematic flow chart of the fabrication procedure consisting of the laser welded/embedded 2D Ag NWs network, solution-based thin PI, and organic/inorganic hybrid GI for a highly flexible TFT platform. b) 2D AFM images of the Ag NWs as-deposited either on a rigid glass substrate, i.e., not embedded (top), or partially embedded in the PI substrate (bottom). c) Topological line profile data obtained along the black/blue dashed lines in (b). d) Photograph of the bent flexible MoS_2 TFTs array. A transparent PET film was laminated under the PI. The inset shows the schematic layer-by-layer structure of the flexible MoS_2 TFT.

separated from the carrier substrate. Finally, a transparent PET film is laminated beneath the PI substrate as a supportive layer.

Figure 1b compares the atomic force microscope (AFM) images of as-deposited, normal (i.e., not-embedded) Ag NWs on a rigid glass substrate and partially embedded Ag NWs in a PI substrate. Individual NWs are clearly identified in the top AFM image in Figure 1b. However, the surface morphology and roughness change dramatically when the Ag NWs are partially embedded in the PI, exhibiting a much smoother surface with reduced roughness as shown in the bottom AFM image in Figure 1b. These results are also confirmed in the topological line profile (Figure 1c). Root-mean-squared heights for normal and embedded Ag NWs are found to be ≈39.0 nm and 6.0 nm, respectively. Figure 1d shows a photograph of a bent MoS_2 TFTs array on flexible PI.

2.2. Plasmonic Laser-Welded Ag NWs Network

Figure 2a illustrates a schematic concept of the laser welding process for the 2D random networks of Ag NWs. In the present work, as-prepared 2D Ag NWs networks exhibit unfavorable electrical sheet resistance, 480–550 Ω sq^{-1}, due to the weak physical contact between each single NW (left-bottom inset of Figure 2a). Here, even though different sheet resistance values can be obtained by tuning the diameter, length, and surface coverage of NWs,[21] a laser process in ambient conditions is applied in order to enhance the electrical properties of the interconnected wires (right-bottom inset of Figure 2a), without elaborately controlling the Ag NW dimensions and areal density.

Upon laser irradiation, the sheet resistance drops drastically to about 10–15 Ω sq^{-1}; the values were almost 37- or 55-fold lower than those of the as-prepared network. Scanning electron microscopy (SEM) images before and after laser irradiation are shown in Figure 2b,c. The results clearly indicate that the laser process forms well-bonded NW junctions (red circle and arrows in Figure 2c) in contrast to the as-prepared NW junctions (Figure 2b). The laser welding process generating the interconnected network is well described by plasmonic laser energy coupling across the minute air gaps naturally formed at the Ag NW junctions.[17,18] The plasmonic light intensity enhancement at the NW junctions enables selective and effective focusing of the laser, thereby inducing localized heating that is sufficient to melt the outer surface of the NWs at the contact. Experimental evidence of such phenomena resulting from local plasmonic effects can be observed in the morphological changes in the NWs. As shown in the inset of Figure 2c, after the laser illumination, the morphology changes substantially at the NW junctions only; the NWs melt slightly and bond to each other. On the other hand, the morphology of NWs away from the junctions appears unaffected, confirming the localized and spatially confined heating. Therefore, the laser welding process differs from conventional blanket thermal heating, which affects the entire system. This local plasmonic effect also helps to minimize damage that could be induced in the heat sensitive organic substrate.[17]

© 2016 WILEY-VCH Verlag GmbH & Co. KGaA, Weinheim

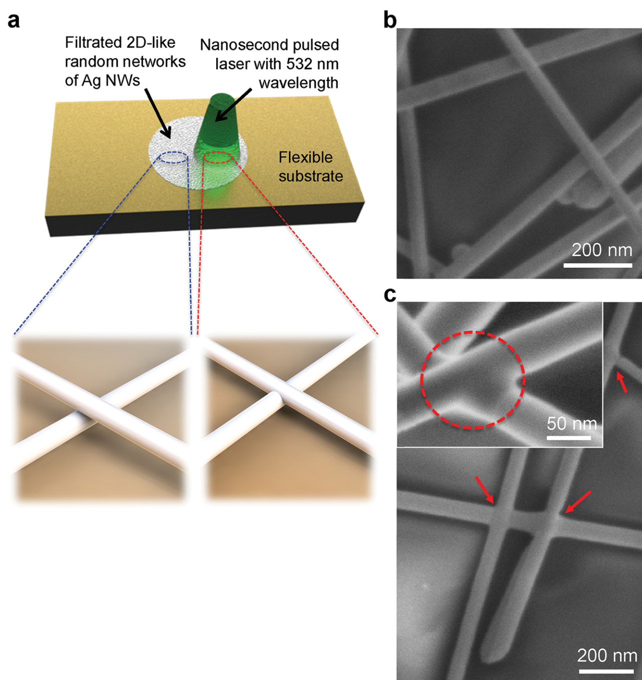

Figure 2. Plasmonic laser welded Ag NWs network for flexible gate electrode. a) The schematic concept of the laser welding process for an Ag NW network that was formed on the PI substrate using the filtration method. The bottom insets show schematic illustrations of the junctions between two adjacent NWs (left) before and (right) after laser treatment. b,c) SEM images of as-prepared Ag NWs random networks before laser welding (b) and after the laser treatment ((c), red arrows indicate the laser welded junctions). The inset shows the magnified SEM image of the laser welded part.

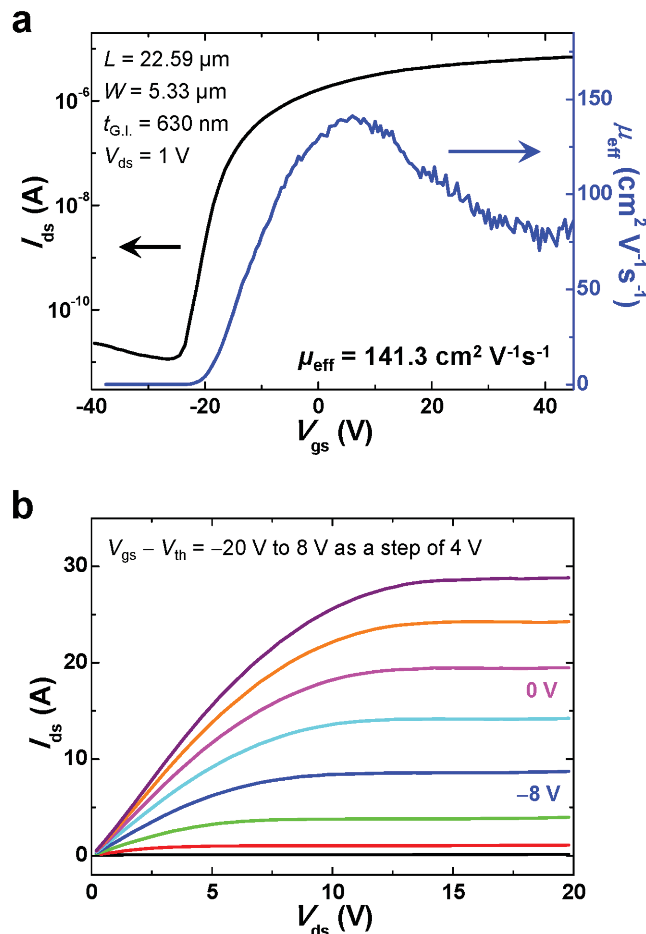

Figure 3. Electrical properties of flexible MoS_2 TFT under initial flat (not bend) condition. a) Transfer characteristic curve (I_{ds}–V_{gs}) and field-effect mobility (μ_{eff}) of the flexible MoS_2 TFT at V_{ds} = 1 V. b) Output characteristics (I_{ds}–V_{ds}) of the same TFT under different gate biases ($V_{gs} - V_{th}$ = −20 to 8 V with 4 V increments).

2.3. Device Characteristics under Unstressed Condition

Figure 3 presents the current–voltage characteristics of the as-detached MoS_2 TFT on PI under the initial flat (i.e., not bent) condition. The thickness of the multilayer MoS_2 is estimated to be 79.3 ± 10.75 nm (see Figure S1 in the Supporting Information). As shown in the transfer (I_{ds}–V_{gs}) characteristic curve (Figure 3a), the flexible MoS_2 TFT exhibits a typical *n*-type behavior,[22] and relatively high I_{on}/I_{off} value greater than 5 × 10^5. It should be noted that the hybrid GI with double-layered structure composed of organic SU-8 and ALD Al_2O_3 provides outstanding barrier properties, which may be the reason for the high performance of our devices (see Figure S2 in the Supporting Information). The μ_{eff} can be calculated from $\mu_{eff} = Lg_m/WC_{GI}V_{ds}$, where L and W are the channel length (22.59 μm) and width (5.33 μm), g_m is the transconductance ($g_m = \partial I_{ds}/\partial V_{gs}|_{V_{ds}} = 1\text{V}$) of 1.55 × 10^{-7} S at V_{gs} = 6.0 V, and C_{GI} is the total capacitance of the hybrid GI with an overall thickness of 630 nm, respectively (see the Supporting Information for the calculation of C_{GI}). A maximum value of μ_{eff} is estimated to be 141.3 cm^2 V^{-1} s^{-1} in linear regime (V_{ds} = 1 V), and statistical distribution of device performances for 12 representative flexible MoS_2 TFTs is also discussed in the Supporting Information in more details. Our multilayer MoS_2 TFTs fabricated with the hybrid GI exhibit much higher mobility than those fabricated with only an ALD Al_2O_3 GI.[8c,d] Fuhrer and co-workers reported similar results comparing MoS_2 TFTs on PMMA GI with those using on silicon dioxide GI.[23] The mobility of the MoS_2 TFTs fabricated on PMMA was higher by approximately an order of magnitude, and this was attributed to the long-range dielectric screening effect,[23,24] which agreed well with the results presented in this work. The output (I_{ds}–V_{ds}) characteristic curves of the same device reveal that Ohmic contacts between the active layer and S/D electrodes is established, as seen in the linear behavior at low V_{ds} regime (Figure 3b). Also, the robust current saturation due to the pinch-off environments at high V_{ds} regime indicates good performance of our flexible MoS_2 TFT, which was also attributed to the postannealing effect (see Figure S4 in the Supporting Information).

2.4. Numerical Simulation of Nonlinear Hyperelastic Materials

The mechanical behavior of hyperelastic materials (e.g., PI, PEN, PET, polymer, or rubber-like materials) is generally expressed in terms of strain energy potential. Furthermore, many different models have been suggested to define the strain

© 2016 WILEY-VCH Verlag GmbH & Co. KGaA, Weinheim

energy function for predicting the properties of hyperelastic materials.[25] Therefore, in order to come up with a proper model describing the mechanical characteristics of the flexible MoS_2 devices, different hyperelastic models must be compared with the real experimental data. **Figure 4**a shows the measured stress (σ)–stretch (λ) curve of a specimen with a thickness (t) of 0.105 mm, fabricated with solution-based PI and PET. Under static and cyclic bending test, the strain (σ) represents the amount of force per unit area, and the engineering stretch (λ) represents the relative elongation

$$\lambda = \frac{(L_0 + \Delta L)}{L_0} = 1 + \varepsilon \tag{1}$$

where ε is the engineering normal strain. From the experimental data, an ultimate tensile stress of 46.6 × 10^6 N m^{-2} is observed at a maximum elongation of 43% (λ = 1.43). Also, within the moderate strain range of interest (<10%, λ = 1.10), the Mooney–Rivlin model is found to match well with our experimental data as shown in the inset of Figure 4a. The two-parameter Mooney–Rivlin model assumes that the local strain energy density in an incompressible material is a simple function of local strain invariants. For uniaxial loading, the nominal stress–stretch behavior for the Mooney–Rivlin model is given by

$$\sigma = \frac{F}{A_0} = 2\left(C_{10} + \frac{C_{01}}{\lambda}\right)\left(\lambda - \frac{1}{\lambda^2}\right) \tag{2}$$

where A_0 is the cross-section area of the test specimen and L_0 is the original length of the specimen. The two-parameters, C_{10} and C_{01}, are material parameters determined by fitting the model (Equation (2)) to the experimental data (blue dot in the inset of Figure 4a). Through the model, the stress state in a cross section of the flexible substrate mounted on a mechanical bending tester can be simulated, as shown in Figure 4b. To investigate the flexible structure, hyperelastic nonlinear stress analysis is performed using the COMSOL Multiphysics module. It is generally known that when an elastomeric slab is bent with arbitrary radius r, there exists a neutral plane (i.e., stress-free zone) in the geometric mid-plane.[26] The computational result shows that the outer surface of the specimen is under tensile stress and the inner surface is under compression, with respect to the neutral plane where the material experiences no stress (Figure 4b). When the bending radius (r) was 5 mm, the maximum internal tensile stress induced in the outermost region (interface between Ag NWs network and PI substrate) is 4.38 × 10^6 N m^{-2}. This induces a total strain of 0.2% in the substrate. Such small strain induced in the PI upon bending indicates that the devices also undergo relatively small mechanical strain levels, hence only slightly affecting the electrical properties. To understand the correlation between the bending radius and the induced stress in detail, calculations were performed with respect to the bending radius and the substrate thickness. Through such a procedure, one may predict a range of device dimensions over which the system is mechanically stable. As shown in Figure 4c, the flexible structure is

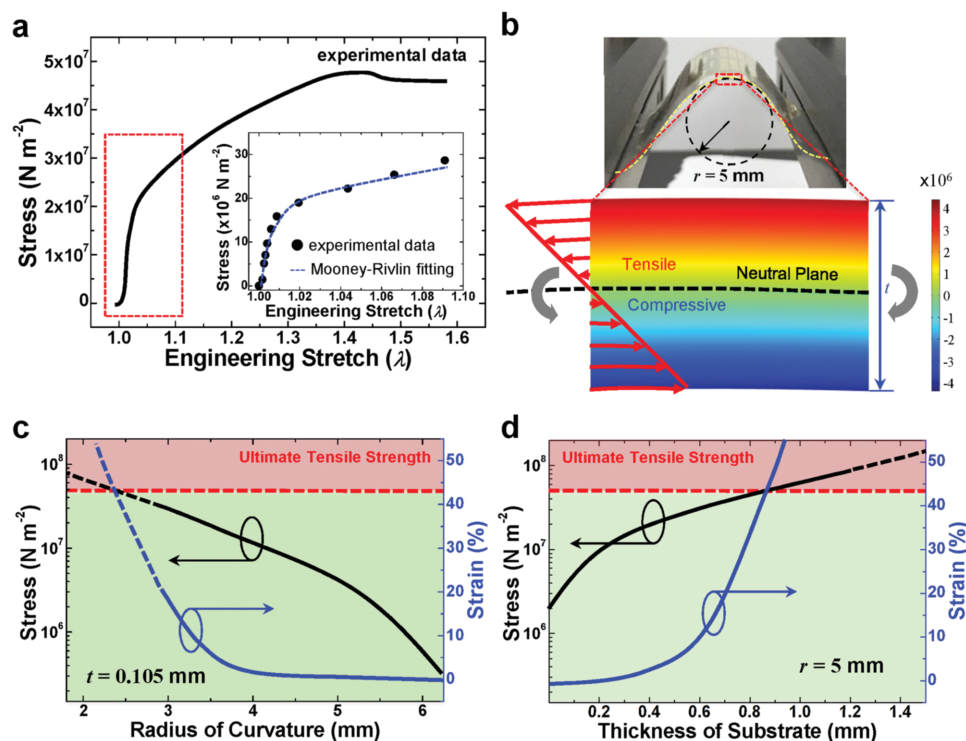

Figure 4. Computational nonlinear hyperelastic analyses on the mechanical bending stress of the flexible MoS_2 TFT. a) Measured stress (σ)–stretch (λ) curve of the specimen of solution-based PI and PET (t = 0.105 mm). The inset shows experimental data fitted with Mooney–Rivlin model. b) The numerical result on hyperelastic nonlinear stress analyses based on the parameters extracted from the experimental data when the bending radius is 5 mm. The top inset shows a photograph of the bent MoS_2 TFTs with a radius of 5 mm. c,d) Based on the Mooney–Rivlin model, the expected mechanically stable range (green region) of the structure with respect to the radius of curvature of the substrate (c) and thickness of the substrate (d).

© 2016 WILEY-VCH Verlag GmbH & Co. KGaA, Weinheim

anticipated to tolerate a specific range of stress (green region, $r > 2.5$ mm at $t = 0.105$ mm) without reaching the failure stress (4.66×10^7 N m^{-2}) and elongation (43%). Note that the results based on the Mooney–Rivlin model do not guarantee device stability at relatively large strains (marked with dotted lines). Also, when the substrate thickness t is larger than 0.8 mm (at r = 5 mm), the structure can be destroyed (Figure 4d). Therefore, in order to remain in the mechanically stable state, the generated stress must be kept below the ultimate tensile strength (red region). Additional parameters, such as the thickness and mechanical properties of each layer (e.g., dielectric, semiconductor, electrodes, etc.) as well as their structure must also be optimized so that functional devices can be achieved. When ductile materials such as metals having very low elastic region (only 0.2% or 0.3% strain) are used, the structure becomes more vulnerable to bending, necessitating so more meticulous design. In this regard, the laser welded Ag NW network may be preferable over metal layers, not only for flexible but also stretchable electronics.

2.5. Variation of TFT Performances under Mechanical Stresses

For investigating the solid tolerance of our flexible MoS_2 TFTs against mechanical stress, static and cyclic upward bending were applied to the flexible TFT array parallel to their active channels (insets of **Figure 5**a,b). The lamination of a 100 µm thick PET film beneath the PI substrate enables the down-shift of neutral plane in the flexible MoS_2 TFTs array, so that the entire TFT could lie within the tensile-stress zone. As a result, the flexibility of our devices can be investigated under harsher environments. Figure 5a compares the transfer characteristic curves of the MoS_2 TFTs array under flat and statically bent conditions. The I_{ds}–V_{gs} curves of the MoS_2 TFT with bending radii of 10 and 5 mm did not change significantly with respect to that in the flat condition. The variation of the mobility values ($\Delta\mu$ (%) = $|\mu_{bending} - \mu_{flat}|/\mu_{flat}$) due to the bending with r = 10 and 5 mm is estimated to be 2.0% and 8.8%, respectively (Figure 5c). The threshold voltage (V_{th}) of the MoS_2 TFT in the flat condition is –18.7 V. For r = 10 mm, the V_{th} just remains identical to its initial value, and shifts to –19.5 V when r = 5 mm. Figure 5b shows a comparison of the transfer characteristics of another MoS_2 TFT under cyclic bending. As the number of bending cycles (n) increases, the entire I_{ds}–V_{gs} curves shift slightly toward negative V_{gs} value. However, the I_{on}/I_{off} ratio is preserved to ≈10^5. The $\Delta\mu$ (V_{th}) due to the cyclic bending with n of 20, 100, and 1000 is 1.9% (–10.1 V), 5.3% (–11.3 V), and 10.0% (–15.4 V), respectively (Figure 5d). It should be noted that the thin ALD Al_2O_3 layer in hybrid GI plays an important role in our flexible TFTs array, by enhancing the adhesion between the GI and the S/D electrodes as well as active layer. MoS_2 TFTs without

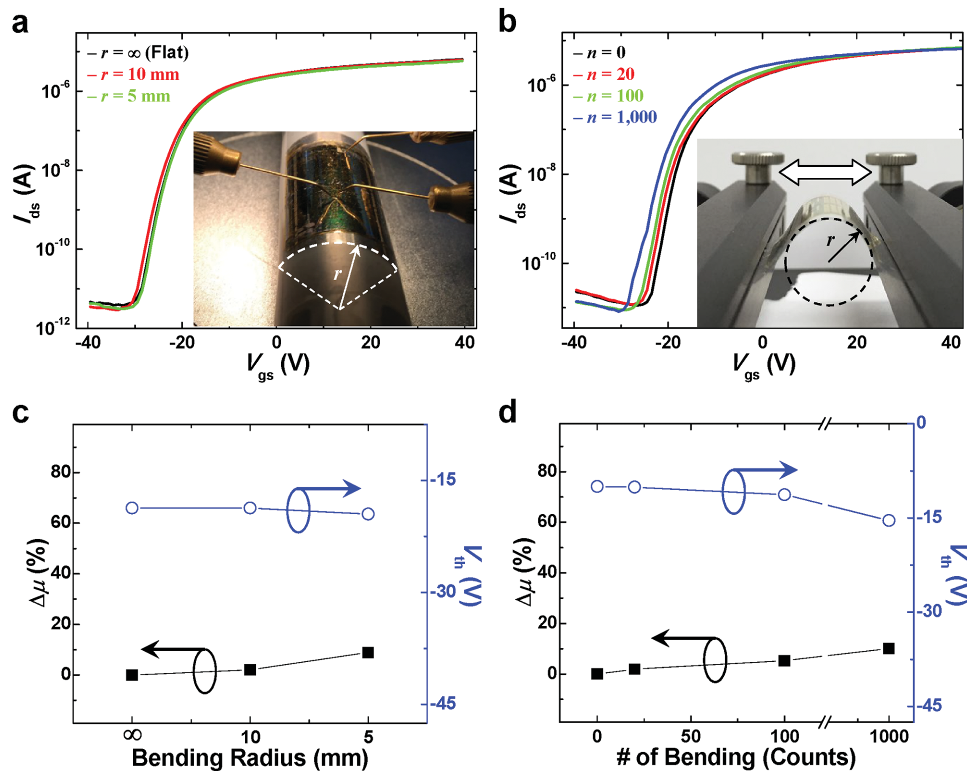

Figure 5. Variation of the flexible MoS_2 TFT performances under various mechanical stresses. a) Comparison of the transfer characteristics of the flexible MoS_2 TFTs under static bending environments with three different bending radii (flat, r = 10 and 5 mm). The inset shows a photograph of the bent MoS_2 TFTs attached on rigid cylinder with a predefined radius (white dashed arc and arrow). b) Comparison of the transfer characteristics under cyclic bending with respect to the number of bending cycles (n = 0, 20, 100, and 1000). The inset shows a photograph of the flexible MoS_2 TFTs loaded on a multimodal bending tester. The cyclic bending radius was fixed at 10 mm (black dashed circle and arrow). c,d) Variations of μ_{eff} and V_{th} of the flexible MoS_2 TFTs as a function of the (c) static bending radii and (d) the number of cyclic bending.

© 2016 WILEY-VCH Verlag GmbH & Co. KGaA, Weinheim

FULL PAPER

Table 1. Comparison of the typical features in various flexible MoS_2 TFTs.

Active MoS_2	Flexible substrate	GI	Electrodes	μ_{eff} / μ_0[a)] [$cm^2 V^{-1} s^{-1}$]	I_{on}/I_{off}	Ref.
CVD, 3-layer	PI	Ion gel	S/D: Ni/Au, G: Ni/Au	3	10^3	[27]
Exfoliated [10 nm]	PI on Kapton film	Al_2O_3 or HfO_2	S/D: Ti/Au, G: Ti/Pd	30[a)]	10^7	[2a]
Exfoliated, 3-layer	PEN	*h*-BN	S/D: Ti/Au, G: graphene	29	10^5	[28]
Exfoliated [3.5 nm]	PI	Al_2O_3	S/D: Au, G: Cu	19[a)]	10^6	[7b]
Exfoliated [58 nm]	PET	*c*-PVP	S/D: graphene, G: ITO	4.7 ± 3.3	$\approx 5 \times 10^4$	[29]
CVD, 1-layer	HfO_2 passivated PI	Al_2O_3	S/D: graphene, G: Au	18.9 ± 1.1[a)]	10^7	[30]
CVD, 1-layer	HfO_2 passivated PI	HfO_2	S/D: Ag/Au, G: Pd	22[a)]	10^5	[31]
Exfoliated [79.3 nm]	PI	SU-8/Al_2O_3	S/D: Ti/Au, G: Ag NWs[b)]	141.3	5×10^5	This work

[a)]Low-field mobility (μ_0) extracted using *Y*-function method; [b)]Laser-welded Ag NWs bilaterally embedded between PI substrate and SU-8 layer.

Al_2O_3 layer exhibited much poorer transistor performances even under less severe bending environments (see Figure S5 in the Supporting Information for more details).

3. Conclusion

In this work, the following configurations were identified as necessary for achieving high electrical performance and mechanical robustness of flexible TFTs: (1) a solution-based PI film (as the substrate), (2) a laser welded 2D random network of Ag NWs embedded in the structure (as the gate electrode), (3) an organic material (SU-8) with ALD Al_2O_3 on top of it (as the gate insulator), and (4) a multilayer MoS_2 (as the channel). Laser irradiation induced plasmonic energy coupling of spatially confined enhanced optical field intensity and localized thermal effects at the junctions of Ag NWs. Because of this effect, the NWs fused only at the junctions without affecting the overall morphology of the entire mesh. SEM images and electrical measurements support the fact that the laser welding process is indeed different from conventional furnace heating processes. Furthermore, the local heating is compatible with plastic substrates with low thermal tolerance. After the laser welding process, the sheet resistance improved significantly (from 480–550 Ω sq^{-1} to 10–15 Ω sq^{-1}, decreasing by almost 37 or 55-fold). In addition, the use of a solution-based PI and flexible hybrid dielectric layers combining organic SU-8 with inorganic Al_2O_3 enabled the fabrication of a solid platform. Numerical computations based on the experimental data (σ–λ) of the specimen (PI laminated on PET film) and bending tests indicate that our designed flexible MoS_2 transistors are resistant to mechanical stress, exhibiting high flexibility. The electrical performance of the devices is not greatly affected during the bending test, both under static and cyclic modes. Further improvements in the device flexibility are expected if an additional protective layer of appropriate thickness is applied on top of the device stack, so that the neutral plane lies in a stress-vulnerable position of the current device. **Table 1** presents a list of typical features of the flexible MoS_2 TFTs in recent reports along with those in our device. As compared in Table 1, the overall results presented in this study make the flexible MoS_2 TFTs attractive for a broad range of electronic applications where high mechanical flexibility is demanded.

4. Experimental Section

Fabrication of Flexible TFT: To construct the Ag NW network, a vacuum transfer method was applied since the vacuum suction pressure can distribute the normal force uniformly on the substrate.[17] First, a Teflon filter (SterliTech, 0.2 µm pore size and 47 mm in diameter) was placed at the neck of a side arm flask connected to a vacuum pump and the glass cap was put on the Teflon filter for the filtration. Then, 25 µL of Ag NW solution (Seashell Technology, with 25 ± 10 µm length and 30 ± 10 nm diameter) dispersed in sufficient isopropyl alcohol (as a carrier fluid) was poured into the cap. Note that Ag concentration was around 5.3 mg mL^{-1}. Only Ag NWs were filtered on the Teflon filter. After drying for 3 h, the filtered Ag NWs were directly transferred from the filter to the target substrate (Glass-1 in Figure 1a) with a uniform normal pressure for 1–2 h. Owing to very low surface energy of Teflon, most of the Ag NWs were transferred easily and a uniform 2D Ag NWs percolation network was formed on the target substrate. The as-prepared Ag NWs had rough contacts that are susceptible to shear force and can result in high contact resistance. Therefore, to enhance the electrical property by forming good contacts, a laser beam with 532 nm wavelength (Solo I Nd:YAG, New Wave) was irradiated onto the Ag NWs network. Also, through an objective lens, the effective area was scaled up to ≈cm scale by an out-of-focal-plane process with a maximum laser energy of 20 mJ.

For a flexible substrate, PI solution was spin-coated on the surface of the laser-welded Ag NWs at 3000 rpm for 30 s and thermally solidified at 60 °C for 30 min. The Ag NWs-embedded PI layer was mechanically detached from the Glass-1 and attached on the carrier substrate (Glass-2) upside down with 3M tape at each corner. The organic GI with a thickness of 600 nm was formed by spin-coating SU-8 2000.5 (Microchem) onto the Ag NWs gate electrode (3000 rpm for 30 s), followed by baking at 110 °C for 5 min and 130 °C for 5 min.

© 2016 WILEY-VCH Verlag GmbH & Co. KGaA, Weinheim

Then, a 30 nm thick amorphous Al_2O_3 was deposited by ALD (Lucida D100, South Korea) with trimethylaluminum as an Al precursor and H_2O as an oxidant. Mechanically exfoliated multilayered MoS_2 flakes were transferred onto the Al_2O_3 film. After E-beam evaporation of a Ti/Au (20/100 nm) layer, S/D electrodes were fabricated by conventional photolithography and etching techniques. The as-fabricated multilayer MoS_2 TFTs on flexible PI substrate were postannealed at 150 °C for 2 h in a vacuum oven ($\leq 10^{-3}$ torr) in order to reduce the contact resistance between the active layer and the S/D electrodes. Transparent PET film with a thickness of 100 µm, as a protective as well as supportive layer for the flexible MoS_2 TFTs, was laminated beneath the PI layer with the aid of an acrylate resin-based pressure sensitive adhesive after the separation of the flexible MoS_2 TFTs from the carrier substrate.

Characterization: The formation of the 2D random network of Ag NWs and contact properties of adjacent NWs due to the laser welding were investigated by field-emission SEM (Nova NanoSEM650, FEI, USA). The surface morphologies of Ag NWs with and without embedded them in the PI was compared by AFM (XE7 Atomic Force Microscope, Park Systems, South Korea) under noncontact mode with a 0.2 Hz scan rate. The stress–stretch curve of the PI and PET films was measured by a mini tensile tester (MICROTEST 200N, UK) with a home-made horizontal moving stage. The electrical properties of the flexible MoS_2 TFTs were measured using a semiconductor characterization system (Keithley 4200 SCS), equipped with a probe station at room temperature under atmospheric environments.

For static bending, the flexible MoS_2 TFTs array was attached onto the surface of rigid cylinders with predefined radii (r = 10 and 5 mm), and electrical properties were investigated in that configuration (inset of Figure 5a). For cyclic bending, the number of bending cycles as well as the bending radius was controlled using a multimodal bending tester (Covotech Co., Ltd, South Korea), as shown in the inset of Figure 5b. The radii under cyclic bending were determined through tangential contact of the rigid cylinder with different dimensions, and the change of the electrical properties due to the cyclic bending was measured under re-flat condition.

Supporting Information

Supporting Information is available from the Wiley Online Library or from the author.

Acknowledgements

W.G.S., H.-J.K., and J.P. contributed equally to this work. This research was supported in part by the National Research Foundation of Korea (NRF-2013M3C1A3059590, NRF-2014M3A9D7070732, 2012R1A1A1042630, and NRF-2015R1A5A1037548). Support by the US Air Force Office of Scientific Research AFOSR/AOARD under Grant FA2386-13-4123 is gratefully acknowledged.

Received: November 23, 2015
Revised: January 11, 2016
Published online: February 9, 2016

[1] a) S. R. Forrest, *Nature* **2004**, *428*, 911; b) G. Crawford, *Flexible Flat Panel Displays*, John Wiley & Sons, Chichester **2005**; c) D. Akinwande, N. Petrone, J. Hone, *Nat. Commun.* **2015**, *5*, 5678.
[2] a) H. Y. Chang, S. Yang, J. Lee, L. Tao, W. S. Hwang, D. Jena, N. Lu, D. Akinwande, *ACS Nano* **2013**, *7*, 5446; b) R. Cheng, S. Jiang, Y. Chen, Y. Liu, N. Weiss, H. C. Cheng, H. Wu, Y. Huang, X. Duan, *Nat. Commun.* **2014**, *5*, 5143; c) J. Pu, L. J. Li, T. Takenobu, *Phys. Chem. Chem. Phys.* **2014**, *16*, 14996; d) W. Zhu, M. N. Yogeesh, S. Yang, S. H. Aldave, J. S. Kim, S. Sonde, L. Tao, N. Lu, D. Akinwande, *Nano Lett.* **2015**, *15*, 1883.
[3] a) K. J. Allen, *Proc. IEEE* **2005**, *93*, 1394; b) K. Jain, M. Klosner, M. Zemel, S. Raghunandan, *Proc. IEEE* **2005**, *93*, 1500; c) M. C. Choi, Y. Kim, C. S. Ha, *Prog. Polym. Sci.* **2008**, *33*, 581.
[4] a) M. Kaltenbrunner, M. S. White, E. D. Głowacki, T. Sekitani, T. Someya, N. S. Sariciftci, S. Bauer, *Nat. Commun.* **2012**, *3*, 770; b) X. Peng, L. Peng, C. Wu, Y. Xie, *Chem. Soc. Rev.* **2014**, *43*, 3303; c) X. Wang, X. Lu, B. Liu, D. Chen, Y. Tong, G. Shen, *Adv. Mater.* **2014**, *26*, 4763.
[5] a) A. N. Sokolov, M. E. Roberts, Z. Bao, *Mater. Today* **2009**, *12*, 12; b) C. Pang, G. Y. Lee, T. I. Kim, S. M. Kim, H. N. Kim, S. H. Ahn, K. Y. Suh, *Nat. Mater.* **2012**, *11*, 795; c) B. C. K. Tee, C. Wang, R. Allen, Z. Bao, *Nat. Nanotechnol.* **2012**, *7*, 825; d) C. Wang, D. Hwang, Z. Yu, K. Takei, J. Park, T. Chen, B. Ma, A. Javey, *Nat. Mater.* **2013**, *12*, 899; e) M. Segev-Bar, H. Haick, *ACS Nano* **2013**, *7*, 8366; f) S. Gong, W. Schwalb, Y. Wang, Y. Chen, Y. Tang, J. Si, B. Shirinzadeh, W. Cheng, *Nat. Commun.* **2014**, *5*, 3132; g) J. Kim, M. Lee, J. S. Rhim, P. Wang, N. Lu, D. H. Kim, *Biomed. Eng. Lett.* **2014**, *4*, 95.
[6] a) Y. Xu, *IEEE Sens. J.* **2013**, *13*, 3962; b) S. J. Benight, C. Wang, J. B. H. Tok, Z. Bao, *Prog. Polym. Sci.* **2013**, *38*, 1961; c) G. Schwartz, B. C. K. Tee, J. Mei, A. L. Appleton, D. H. Kim, H. Wang, Z. Bao, *Nat. Commun.* **2013**, *4*, 1859; d) W. Zeng, L. Shu, Q. Li, S. Chen, F. Wang, X. M. Tao, *Adv. Mater.* **2014**, *26*, 5310.
[7] a) S. Bertolazzi, J. Brivio, A. Kis, *ACS Nano* **2011**, *5*, 9703; b) G. A. Salvatore, N. Münzenrieder, C. Barraud, L. Petti, C. Zysset, L. Büthe, K. Ensslin, G. Tröster, *ACS Nano* **2013**, *7*, 8809.
[8] a) B. Radisavljevic, A. Radenovic, J. Brivio, V. Giacometti, A. Kis, *Nat. Nanotechnol.* **2011**, *6*, 147; b) Q. H. Wang, K. Kalantar-Zadeh, A. Kis, J. N. Coleman, M. S. Strano, *Nat. Nanotechnol.* **2012**, *7*, 699; c) W. Choi, M. Y. Cho, A. Konar, J. H. Lee, G. B. Cha, S. C. Hong, S. Kim, J. Kim, D. Jena, J. Joo, S. Kim, *Adv. Mater.* **2012**, *24*, 5832; d) S. Kim, A. Konar, W. S. Hwang, J. H. Lee, J. Lee, J. Yang, C. Jung, H. Kim, J. B. Yoo, J. Y. Choi, Y. W. Jin, S. Y. Lee, D. Jena, W. Choi, K. Kim, *Nat. Commun.* **2012**, *3*, 1011; e) M. Chhowalla, H. S. Shin, G. Eda, L. J. Li, K. P. Loh, H. Zhang, *Nat. Chem.* **2013**, *5*, 263.
[9] a) M. Hasegawa, K. Horie, *Prog. Polym. Sci.* **2001**, *26*, 259; b) K. L. Mittal, *Polyimides: Synthesis, Characterization, and Applications*, Springer Science & Business Media, New York **2013**.
[10] a) J. Y. Kim, J. H. Jung, D. E. Lee, J. Joo, *Synth. Met.* **2002**, *126*, 311; b) J. Ouyang, Q. Xu, C. W. Chu, Y. Yang, G. Li, J. Shinar, *Polymer* **2004**, *45*, 8443; c) U. Lang, E. Muller, N. Naujoks, J. Dual, *Adv. Funct. Mater.* **2009**, *19*, 1215.
[11] B. Y. Ahn, D. J. Lorang, J. A. Lewis, *Nanoscale* **2011**, *3*, 2700.
[12] a) J. Wu, H. A. Becerril, Z. Bao, Z. Liu, Y. Chen, P. Peumans, *Appl. Phys. Lett.* **2008**, *92*, 263302; b) G. Eda, G. Fanchini, M. Chhowalla, *Nat. Nanotechnol.* **2008**, *3*, 270; c) K. S. Kim, Y. Zhao, H. Jang, S. Y. Lee, J. M. Kim, K. S. Kim, J. H. Ahn, P. Kim, J. Y. Choi, B. H. Hong, *Nature* **2009**, *457*, 706.
[13] a) M. Kaempgen, G. S. Duesberg, S. Roth, *Appl. Surf. Sci.* **2005**, *252*, 425; b) K. A. Watson, S. Ghose, D. M. Delozier, J. G. Smith Jr, J. W. Connell, *Polymer* **2005**, *46*, 2076.
[14] a) F. M. Blighe, Y. R. Hernandez, W. J. Blau, J. N. Coleman, *Adv. Mater.* **2007**, *19*, 4443; b) S. De, P. E. Lyons, S. Sorel, E. M. Doherty, P. J. King, W. J. Blau, P. N. Nirmalraj, J. J. Boland, V. Scardaci, J. Joimel, J. N. Coleman, *ACS Nano* **2009**, *3*, 714; c) Z. Yu, X. Niu, Z. Liu, Q. Pei, *Adv. Mater.* **2011**, *23*, 3989.
[15] a) J. Y. Lee, S. T. Connor, Y. Cui, P. Peumans, *Nano Lett.* **2008**, *8*, 689; b) S. De, T. M. Higgins, P. E. Lyons, E. M. Doherty, P. N. Nirmalraj, W. J. Blau, J. J. Boland, J. N. Coleman, *ACS Nano* **2009**, *3*, 1767; c) L. Hu, H. S. Kim, J. Y. Lee, P. Peumans, Y. Cui, *ACS Nano* **2010**, *4*, 2955; d) A. R. Madaria, A. Kumar, C. Zhou, *Nanotechnology* **2011**, *22*, 245201.

© 2016 WILEY-VCH Verlag GmbH & Co. KGaA, Weinheim

[16] H. G. Im, S. H. Jung, J. Jin, D. Lee, J. Lee, D. Lee, J. Y. Lee, I. D. Kim, B. S. Bae, *ACS Nano* **2014**, *8*, 10973.
[17] S. Han, S. Hong, J. Ham, J. Yeo, J. Lee, B. Kang, P. Lee, J. Kwon, S. S. Lee, M. Y. Yang, S. H. Ko, *Adv. Mater.* **2014**, *26*, 5808.
[18] E. C. Garnett, W. Cai, J. J. Cha, F. Mahmood, S. T. Connor, M. Greyson Christoforo, Y. Cui, M. D. McGehee, M. L. Brongersma, *Nat. Mater.* **2012**, *11*, 241.
[19] a) H. Lifka, C. Tanase, D. McCulloch, P. Van De Weijer, I. French, *SID. Int. Symp. Dig. Tec.* **2007**, *38*, 1599; b) M. S. Ko, C. Y. Im, I. Lee, J. H. Lee, S. Kim, W. E. Hong, J. S. Ro, *SID. Int. Symp. Dig. Tec.* **2011**, *42*, 118.
[20] a) M. Amjadi, A. Pichitpajongkit, S. Lee, S. Ryu, I. Park, *ACS Nano* **2014**, *8*, 5154; b) W. G. Song, S. Yun, K. Kyung, J. Lee, J. Baek, S. Kim, Y. K. Hong, *J. Nanosci. Nanotechnol.* **2016**, DOI: 10.1166/jnn.2016.12512.
[21] a) J. Lee, P. Lee, H. Lee, D. Lee, S. S. Lee, S. H. Ko, *Nanoscale* **2012**, *4*, 6408; b) S. M. Bergin, Y. H. Chen, A. R. Rathmell, P. Charbonneau, Z. Y. Li, B. J. Wiley, *Nanoscale* **2012**, *4*, 1996; c) S. K. Duan, Q. L. Niu, J. F. Wei, J. B. He, Y. A. Yin, Y. Zhang, *Phys. Chem. Chem. Phys.* **2015**, *17*, 8106.
[22] a) S. Das, H. Y. Chen, A. V. Penumatcha, J. Appenzeller, *Nano Lett.* **2013**, *13*, 100; b) J. Kwon, Y. K. Hong, H. J. Kwon, Y. Jin Park, B. Yoo, J. Kim, C. P. Grigoropoulos, M. Suk Oh, S. Kim, *Nanotechnology* **2015**, *26*, 035202.
[23] W. Bao, X. Cai, D. Kim, K. Sridhara, M. S. Fuhrer, *Appl. Phys. Lett.* **2013**, *102*, 042104.
[24] C. Jang, S. Adam, J. H. Chen, E. D. Williams, S. Das Sarma, M. S. Fuhrer, *Phys. Rev. Lett.* **2008**, *101*, 146805.
[25] H. J. Kwon, H. Shim, S. Kim, W. Choi, Y. Chun, I. Kee, S. Lee, *Appl. Phys. Lett.* **2011**, *98*, 151904.
[26] a) M. Ohring, *The Materials Science of Thin Films*, Academic Press, San Diego, CA **1992**; b) D. H. Kim, J. H. Ahn, M. C. Won, H. S. Kim, T. H. Kim, J. Song, Y. Y. Huang, Z. Liu, C. Lu, J. A. Rogers, *Science* **2008**, *320*, 507; c) D. Kim, G. Shin, Y. J. Kang, W. Kim, J. S. Ha, *ACS Nano* **2013**, *7*, 7975.
[27] J. Pu, Y. Yomogida, K. K. Liu, L. J. Li, Y. Iwasa, T. Takenobu, *Nano Lett.* **2012**, *12*, 4013.
[28] G. H. Lee, Y. J. Yu, X. Cui, N. Petrone, C. H. Lee, M. S. Choi, D. Y. Lee, C. Lee, W. J. Yoo, K. Watanabe, T. Taniguchi, C. Nuckolls, P. Kim, J. Hone, *ACS Nano* **2013**, *7*, 7931.
[29] J. Yoon, W. Park, G. Y. Bae, Y. Kim, H. S. Jang, Y. Hyun, S. K. Lim, Y. H. Kahng, W. K. Hong, B. H. Lee, H. C. Ko, *Small* **2013**, *9*, 3295.
[30] M. Amani, R. A. Burke, R. M. Proie, M. Dubey, *Nanotechnology* **2015**, *26*, 115202.
[31] H.-Y. Chang, M. N. Yogeesh, R. Ghosh, A. Rai, A. Sanne, S. Yang, N. Lu, S. K. Banerjee, D. Akinwande, *Adv. Mater.* **2016**, DOI: 10.1002/adma.201504309.

© 2016 WILEY-VCH Verlag GmbH & Co. KGaA, Weinheim